A Model for Local Impedance: Validation of the Model for Local Parameters Recovery from a Single Spectrum of PEM Fuel Cell

Tatyana Reshetenko[1,*,z] **and Andrei Kulikovsky**[2,*,z]

[1]*Hawaii Natural Energy Institute, University of Hawaii, Honolulu, Hawaii 96822, USA*
[2]*Forschungszentrum Jülich GmbH, Institute of Energy and Climate Research, Electrochemical Process Engineering, D-52425 Jülich, Germany*

A physics–based numerical model for fitting local impedance spectra (local impedance model, LIM) of the segmented PEM fuel cell is developed and used to validate our recent model for recovery of local parameters from a single spectrum of the whole cell (cell impedance model, CIM). Shapes of the local parameters along the cathode channel resulting from the two models are compared. Overall, the CIM quite satisfactorily describes the cell local parameters provided that the oxygen transport impedance in the channel is not small as compared to other impedances in the cell.

[DOI: 10.1149/2.1241906jes]

Manuscript submitted December 12, 2018; revised manuscript received April 3, 2019. Published April 16, 2019.

In real applications, polymer electrolyte membrane fuel cells (PEMFCs) operate at low oxygen stoichiometry, which may cause quite significant non–uniformity of local current density and liquid water content over the cell surface.[1] This, in turn, leads to non–uniformity of transport and kinetic parameters. Understanding the shapes of local parameters is of large interest for cell designers.

Impedance spectra of a PEMFC contain invaluable information on the cell parameters. Every process running in a PEMFC has its own characteristic time constant and hence it gives a contribution to the cell impedance in a frequency range specific to this process.[2] Analysis of impedance spectra allows us, in principle, to separate these contributions and to calculate the respective cell transport and kinetic coefficients.[3] Impedance spectroscopy is a non–destructive and "non–invasive" characterization method; the spectra can be measured in operando in a working fuel cell. These advantages provided exponentially growing interest in this technique: the Scopus database of scientific publications shows that the number of publications on impedance spectroscopy in fuel cells doubles every 4.8 years.

Deciphering of impedance spectra requires modeling. After a pioneering work of Springer et al.,[4] a lot of efforts have been done to develop physics–based models for PEMFC impedance.[5–18] However, most of the models assume that the kinetic and through–plane transport parameters are uniform over the cell surface.

The distribution of local parameters can be obtained from local impedance measurements. However, measuring of local impedance is a complex and expensive technique, which requires segmentation of the cell cathode, multichannel EIS meter, control of the segments current etc.[19–22] On the other hand, a spectrum of the whole cell can be thought of as a certain superposition of local spectra. Is it possible to recover local parameters from a single spectrum of the whole cell?

Recently, a model for such recovery has been proposed.[23] The model is based on the following idea. Consider a cell with the straight cathode channel and let the cathode current collector of this cell be separated into N virtual segments (Figure 1). The local impedances Z_{loc} of individual segments are connected in parallel; however, oxygen transport in the channel generates impedances Z_h, so that the equivalent circuit of the cell consists of repeating elements Z_h and Z_{loc} (Figure 1). It can be shown that due to non–zeros Z_h, the whole spectrum of this system can be used to determine each Z_{loc} and Z_h.[23]

This gives us an opportunity to determine the local cell parameters from a single spectrum of the whole cell. In ,[23] the model has been illustrated by recovering the local cell parameters from the single PEMFC spectrum using a cell impedance model (CIM) and a cell decomposition into 10 and 20 virtual segments. No comparison of directly measured local parameters with the parameters determined from the CIM has been done.

In the present work, we develop a model for fitting experimental local spectra of the segmented cell (local impedance model, LIM). Further, we report validation of the CIM based on comparison of the local parameters determined from the CIM and LIM. In,[24] a low–current analytical model which takes into account transport of the oxygen concentration perturbation c_h^1 in the channel was used for local spectra fitting. This model ignores the impedance due to oxygen transport in the cathode catalyst layer (CCL). In,[25] the local segment spectra have been fitted ignoring transport of c_h^1 in the channel. This corresponds to the situation when segments are excited with the AC signal one–by–one, while all the other segments work in the steady conditions. In our experiments, all the segments are excited simultaneously, and the oxygen concentration perturbation is transported with the flow affecting impedance of the segments located downstream. Below, we take into account this process in the LIM and CIM.

The goal of this work is twofold: first, we report the LIM, and second, we apply the LIM to validate the CIM. Only a few labs in the world have equipment for local impedance measurements in PEMFCs. On the other hand, measuring of the whole cell impedance is a routine technique; along with the polarization curve measurements EIS is considered nowadays as a standard cell testing procedure. Thus, development of the model for recovery of local parameters from the cell spectrum could be of large interest for cell testing and design.

Experimental

Experimental work has been performed using a segmented cell system and a test station developed at Hawaii Natural Energy Institute.[26] The segmented cell setup consists of the cell hardware, current transducer system and data acquisition device. The current transducer system was custom designed and employed closed loop Hall sensors

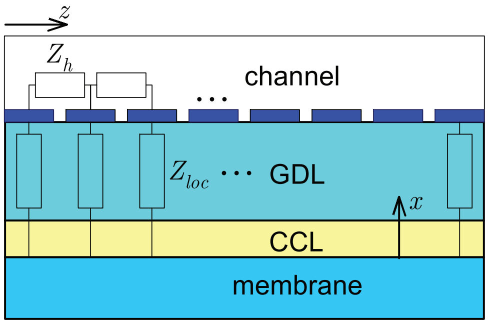

Figure 1. Schematic of the segmented cell and the system of coordinates.

---

[*] Electrochemical Society Member.
[z] E-mail: tatyanar@hawaii.edu; A.Kulikovsky@fz-juelich.de

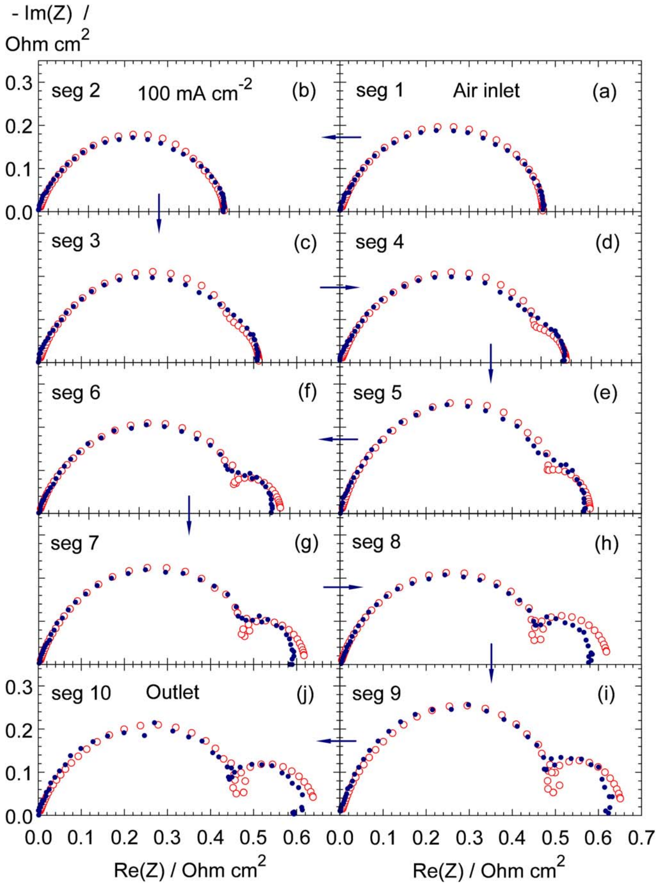

Figure 2. Local experimental (dots) and fitted LIM (open circles) spectra from the segments 1 to 10. The cell current density is 100 mA cm^{-2}. The experimental and model points are indicated for the same frequencies. Arrows indicate direction of the air flow.

(Honeywell CSNN191) for current measurements. The segmented cell system is run as a single cell using the test station and standard operating protocols. This configuration reduces any interferences from the segmented cell setup and provides operating conditions identical to real ones, since only the overall cell load is governed by the test station. The whole system enables simultaneous measurements of local current, voltage and impedance. Details of the segmented cell system can be found in Refs. 26–28.

The segmented cell hardware contains standard non-segmented and segmented flow field plates and a 100 cm^2 MEA. The segmented flow field consists of 10 segments, each of them has an area of 7.6 cm^2, its own current collector and gas diffusion layer (GDL). The air inlet segment is segment 1, while segment 10 is the outlet; the segments form two parallel rows (Figure 2). The system design allows either anode or cathode to be segmented. In this work, the segmentation was applied to the cathode. Both flow field plates have the same ten parallel channel serpentine design. The fuel and oxidant streams are arranged in co–flow configuration.

We used commercially available 100 cm^2 catalyst coated membranes (CCM) provided by Gore. Pt/C loading was 0.4 mg$_{Pt}$ cm^{-2} for anode and cathode with the catalyst layer thickness of 10–12 μm. The thickness of the reinforced membrane varied in the range of 16–18 μm. Sigracet 25 BC was used as GDLs for both electrodes. 25 BC consists of carbon paper and a microporous layer (MPL) with total thickness of 220–235 μm and porosity of 80%. Segmented GDLs were used on the cathode side, whereas a single and uniform GDL was applied at the anode. Teflon gaskets (125 μm) were employed for both electrodes to ensure required compression ratio.

Table I. Geometrical and operating parameters of the cell. A/C stands for anode/cathode.

Catalyst loading A/C, mg$_{Pt}$ cm^{-2}	0.4/0.4
Catalyst layer thickness l_t, μm	12
Gas diffusion layer thickness l_b, μm	235
Channel depth h, cm	0.15
Channel length L, cm	52.78
ORR exchange current density i_*, A cm^{-3} (assumed)	10^{-3}
Parameter β in Eq. 4	7.3
Flow stoichiometry A/C	2/4
Relative humidity A/C	100%/50%
Absolute pressure, A/C, kPa	150/150
Cell temperature, K	273 + 80

The cell was operated with H$_2$/air gas configuration at a temperature of 80°C. The anode/cathode conditions were 2/4 stoichiometry, 100/50% relative humidity and 150/150 kPa absolute pressure. The impedance measurements were performed under galvanostatic control of the cell over the frequency range from 0.05 Hz to 10 kHz with 11 steps per decade. The amplitude of the sinusoidal current perturbation was chosen to get a cell voltage response of 10 mV or lower. The impedance spectra have been recorded simultaneously from 10 segments and from the whole cell. The cell operating and geometrical parameters are listed in Table I. Normally, PEMFCs operate at an air stoichiometry between 1.5 and 2; however, local segment spectra at low stoichiometries are rather noisy, especially at the cell current densities below 100 mA cm^{-2}. Here, for the sake of local and cell model comparison, we perform measurements with the MEA from Gore having high Pt loading at the air stoichiometry of 4. In this regime, the local experimental spectra are much more smooth leading to better quality of spectra fitting.

Models for Local and Cell Impedance

General description of the two models.—Consider a cell with the straight channel and segmented electrodes (Figure 1). The equations forming local and cell impedance models are collected in Section Equations for the Perturbation Amplitudes. Here, we list equations which stand behind the two impedance models.

The models are based on the same system of conservation equations. In the CCL, this system includes the transient proton charge conservation equation, the Ohm's law for proton transport, and the transient oxygen mass balance equation:

$$C_{dl}\frac{\partial \eta}{\partial t} + \frac{\partial j}{\partial x} = -2i_*\left(\frac{c}{c_{ref}}\right)\sinh\left(\frac{\eta}{b}\right) \qquad [1]$$

$$j = -\sigma_0 s\frac{\partial \eta}{\partial x} \qquad [2]$$

$$\frac{\partial c}{\partial t} - D_{ox}\frac{\partial^2 c}{\partial x^2} = -\frac{2i_*}{4F}\left(\frac{c}{c_{ref}}\right)\sinh\left(\frac{\eta}{b}\right) \qquad [3]$$

where

$$s = \exp\left(-\beta x/l_t\right) \qquad [4]$$

describes the variation of proton conductivity through the CCL depth, with β being the characteristic scale of this variation.[29] Note that $\beta = 0$ corresponds to uniform along x conductivity. In Eqs. 1–3, η is the positive by convention oxygen reduction reaction (ORR) overpotential, t is time, x is the distance through the CCL depth counted from the membrane, j is the local proton current density, l_t is the CCL thickness, i_* is the ORR volumetric exchange current density, c and c_{ref} are the local and reference (inlet) oxygen concentrations, b is the ORR Tafel slope, C_{dl} is the double layer volumetric capacitance, σ_0 is the CCL proton conductivity at the membrane interface, and D_{ox} is the effective oxygen diffusion coefficient in the CCL.

Oxygen transport in the GDL is described using the transient diffusion equation:

$$\frac{\partial c_b}{\partial t} - D_b \frac{\partial^2 c_b}{\partial x^2} = 0 \qquad [5]$$

where c_b is the oxygen concentration in the GDL, and D_b is the GDL oxygen diffusivity. The system of Equations 1–5 forms a through–plane sub–model for the performance of each individual segment. The segment sub–models are coupled by the oxygen transport equation in the air channel:

$$\frac{\partial c_h}{\partial t} + v\frac{\partial c_h}{\partial z} = -\left.\frac{D_b}{h}\frac{\partial c_b}{\partial x}\right|_{x=lt+lb} \qquad [6]$$

where z is the distance along the channel, c_h is the oxygen concentration in the channel, v is the flow velocity, h is the channel depth, and l_b is the GDL thickness. The right side of Eq. 6 is the oxygen flux on the GDL side at the channel/GDL interface. Solution to Eq. 6 is used as the boundary condition for the oxygen concentration at the channel/GDL interface in the segment sub–model. Eq. 6 takes into account oxygen transport impedance in the cathode channel. Importance of this “forgotten player” for the PEMFC impedance analysis has been emphasized in experiments of Schneider et al.[30,31]

All the listed above equations are linearized and Fourier–transformed to yield a system of equations for the perturbation amplitudes of the overpotential and oxygen concentration in the porous layers and channel (see the next section). These systems are solved numerically, as described below, and the solution is used to calculate local impedance of each segment Z_{seg}, and impedance of the whole cell Z_{cell}.

The key difference between the LIM and CIM is that in the LIM, calculated Z_{seg} is fitted to the local experimental impedance of this segment, while in the CIM, impedance of the whole cell Z_{cell} is fitted to the measured spectrum of the whole cell. The CIM, thus, ignores the local experimental spectra from individual segments, which corresponds to the usual situation of a non–segmented cell, when only the whole cell impedance is available. This is discussed in more details below.

Equations for the perturbation amplitudes.—In this Section, we list linear equations for the perturbation amplitudes, which form the basis for the LIM and CIM. For the details of these equations derivation from Eqs. 1–6 the reader is referred to Refs. 28,32. In this work, the dimensionless impedance equations are written in the most general form, taking into account that each segment has its own set of parameters. Information in this and the next sections is sufficient to reproduce the models.

The system of equations for the perturbation amplitudes of the ORR overpotential $\tilde{\eta}^1(\tilde{x}, \tilde{\omega})$ and of the oxygen concentration $\tilde{c}^1(\tilde{x}, \tilde{\omega})$ in the CCL is

$$\varepsilon^2 r_\sigma \frac{\partial}{\partial \tilde{x}}\left(s(\tilde{x})\frac{\partial \tilde{\eta}^1}{\partial \tilde{x}}\right) = \sinh\left(\frac{\tilde{\eta}^0}{r_b}\right)\tilde{c}^1 + \left(\frac{\tilde{c}^0}{r_b}\cosh\left(\frac{\tilde{\eta}^0}{r_b}\right) + \mathrm{i}\tilde{\omega} r_{dl}\right)\tilde{\eta}^1,$$

$$\tilde{\eta}^1(1) = \tilde{\eta}^1_1, \quad \left.\frac{\partial \tilde{\eta}^1}{\partial \tilde{x}}\right|_{\tilde{x}=1} = 0 \qquad [7]$$

$$\varepsilon^2 \tilde{D}_{ox}\frac{\partial^2 \tilde{c}^1}{\partial \tilde{x}^2} = \left(\sinh\left(\frac{\tilde{\eta}^0}{r_b}\right) + \mathrm{i}\tilde{\omega}\mu^2\right)\tilde{c}^1 + \frac{\tilde{c}^0}{r_b}\cosh\left(\frac{\tilde{\eta}^0}{r_b}\right)\tilde{\eta}^1,$$

$$\left.\frac{\partial \tilde{c}^1}{\partial \tilde{x}}\right|_{\tilde{x}=0} = 0,$$

$$\tilde{c}^1(1) + \frac{\tan\left(\mu\tilde{l}_b\sqrt{-\mathrm{i}\Omega/\tilde{D}_b}\right)}{\mu\sqrt{-\mathrm{i}\Omega\tilde{D}_b}}\tilde{D}_{ox}\left.\frac{\partial \tilde{c}^1}{\partial \tilde{x}}\right|_{\tilde{x}=1} = \frac{\tilde{c}^1_h}{\cos\left(\mu\tilde{l}_b\sqrt{-\mathrm{i}\Omega/\tilde{D}_b}\right)} \qquad [8]$$

Here, the superscripts 0 and 1 mark the static variables and the small–amplitude perturbations, respectively,

$$r_b = \frac{b}{b_*}, \quad r_{dl} = \frac{C_{dl}}{C^*_{dl}}, \quad r_\sigma = \frac{\sigma_0}{\sigma_*} \qquad [9]$$

and all the variables are nondimenionalized according to

$$\tilde{x} = \frac{x}{l_t}, \quad \tilde{c} = \frac{c}{c_{ref}}, \quad \tilde{\eta} = \frac{\eta}{b_*}, \quad \tilde{\omega} = \frac{\omega C^*_{dl} b_*}{2 i_*},$$

$$\tilde{D}_{ox} = \frac{4FD_{ox}c_{ref}}{\sigma_* b_*}, \quad \tilde{D}_b = \frac{4FD_b c_{ref}}{\sigma_* b_*}, \quad \tilde{Z} = \frac{Z\sigma_*}{l_t} \qquad [10]$$

where ω is the angular frequency of the AC signal, Z is the impedance. The reduced dimensionless frequency Ω and the dimensionless parameters ε and μ are

$$\Omega = \frac{\tilde{\omega}}{\varepsilon^2} = \frac{\omega C^*_{dl} l_t^2}{\sigma_*}, \quad \varepsilon = \sqrt{\frac{\sigma_* b_*}{2 l_t^2 i_*}}, \quad \mu = \sqrt{\frac{4Fc_{ref}}{C^*_{dl} b_*}} \qquad [11]$$

Note that the set of absolute characteristic values b_*, C^*_{dl} and σ_* is used for the normalization. This is necessary, as the parameters b, C_{dl} and σ_0 vary from one segment to another, as discussed below.

The right Robin–type boundary condition for Eq. 8 follows from analytical solution of equation for the oxygen concentration perturbation in the GDL. The dimensionless perturbation amplitude of the oxygen concentration in the channel $\tilde{c}^1_h(\tilde{z}, \tilde{\omega})$ is governed by equation

$$\lambda\tilde{J}\frac{\partial \tilde{c}^1_h}{\partial \tilde{z}} = \left(\mu\sqrt{-\mathrm{i}\Omega\tilde{D}_b}\tan\left(\mu\tilde{l}_b\sqrt{-\mathrm{i}\Omega/\tilde{D}_b}\right) - \mathrm{i}\xi^2\varepsilon^2\Omega\right)\tilde{c}^1_h$$

$$-\frac{\tilde{D}_{ox}\partial\tilde{c}^1/\partial\tilde{x}\big|_{\tilde{x}=1}}{\cos\left(\mu\tilde{l}_b\sqrt{-\mathrm{i}\Omega/\tilde{D}_b}\right)}, \quad \tilde{c}^1_h(0) = 0 \qquad [12]$$

Here, $\tilde{z} = z/L$ is the dimensionless distance along the channel, $\tilde{J} = Jl_t/(\sigma_* b_*)$ is the dimensionless mean current density in the cell,

$$\lambda = \frac{4Fhvc_{ref}}{LJ} \qquad [13]$$

is the oxygen (air) flow stoichiometry, L is the channel length, and ξ is the dimensionless parameter

$$\xi = \sqrt{\frac{8Fhc_{ref}l_t i_*}{C^*_{dl}\sigma_* b_*^2}} \qquad [14]$$

The parameter $\tilde{\eta}^1_1$ which appears in the first boundary condition to Eq. 7 is the amplitude of the applied AC perturbation. For this parameter, any positive non–zero number can be taken, as the impedance is independent of $\tilde{\eta}^1_1$.

The local impedance of the kth segment is calculated according to

$$Z_{seg,k} = -\frac{\eta^1}{\sigma_{0,k}\partial\eta^1/\partial x} \qquad [15]$$

where $\sigma_{0,k}$ is the proton conductivity at the membrane/CCL interface in the kth segment. Finally, in the CIM, the total cell impedance Z_{cell} is calculated from the equation

$$\frac{1}{Z_{cell}} = \frac{1}{N}\sum_{k=1}^{N}\frac{1}{Z_{seg,k}} \qquad [16]$$

where N is the number of segments.

Equations for the static variables.—In every segment, the static shapes of the overpotential $\tilde{\eta}^0$ and $\tilde{c}^0$ through the CCL depth are calculated as follows. First, the system of equations for the static local proton current density $\tilde{j}^0$ and oxygen concentration $\tilde{c}^0$ is solved:

$$\frac{\partial^2 \tilde{j}^0}{\partial \tilde{x}^2} = \left(\frac{\tilde{j}_0 - \tilde{j}^0}{\tilde{D}_{ox}\tilde{c}^0} - \frac{\tilde{j}^0}{r_\sigma r_b s(\tilde{x})}\right)\frac{\partial \tilde{j}^0}{\partial \tilde{x}}, \quad \tilde{j}^0(0) = \tilde{j}_0, \quad \tilde{j}^0(1) = 0 \qquad [17]$$

$$\tilde{D}_{ox}\frac{\partial \tilde{c}^0}{\partial \tilde{x}} = \tilde{j}_0 - \tilde{j}^0, \quad \tilde{c}^0(1) = \tilde{c}^0_h - \frac{\tilde{j}_0 \tilde{l}_b}{\tilde{D}_b}, \qquad [18]$$

where $\tilde{j}_0 \equiv \tilde{j}^0_0(\tilde{z})$ is the static local cell current density. With $\tilde{c}^0$ and $\tilde{j}^0$ at hand, the shape of the static overpotential is calculated as

$$\tilde{\eta}^0 = -\text{arcsinh}\left(\frac{\varepsilon^2}{\tilde{c}^0}\frac{\partial \tilde{j}^0}{\partial \tilde{x}}\right). \qquad [19]$$

In Eqs. 17, 18, the static shapes of $\tilde{j}_0(\tilde{z})$ and of the oxygen concentration $\tilde{c}^0_h(\tilde{z})$ can be estimated as

$$\tilde{c}^0_h = \left(1 - \frac{1}{\lambda}\right)^{\tilde{z}}, \quad \tilde{j}_0 = -\lambda \ln\left(1 - \frac{1}{\lambda}\right)\left(1 - \frac{1}{\lambda}\right)^{\tilde{z}} \tilde{J}, \qquad [20]$$

provided that the cell current density is below 100 mA cm^{-2}. For larger currents, these shapes can be calculated as discussed in Refs. 33,34. If experimental data on the shape of the local cell current are available, $\tilde{j}_0(\tilde{z})$ can be obtained by spline interpolation of the measured points. The function $\tilde{c}^0_h(\tilde{z})$ is then determined from the static version of Eq. 6:

$$\lambda \tilde{J} \frac{\partial \tilde{c}^0_h}{\partial \tilde{z}} = -\tilde{j}_0(\tilde{z}), \quad \tilde{c}^0_h(0) = 1 \qquad [21]$$

In this work, for the sake of CIM validation, in both LIM and CIM we used the experimental data on $\tilde{j}_0(\tilde{z})$ and Eq. 21 to calculate $\tilde{c}^0_h(\tilde{z})$.

Numerical details.—Eqs. 7 and 8 form a model for local impedance of an individual segment. The right boundary condition to Eq. 8 includes the oxygen transport in the GDL, and the perturbation of local oxygen concentration $\tilde{c}^1_h$ in the cathode channel at the segment of interest. The value of $\tilde{c}^1_h$ obeys to the transport Equation 12, which "links" the segments. Therefore, to solve the system 7, 8, we have to solve Eq. 12 first. However, Eq. 12 contains the oxygen flux perturbation at the CCL/GDL interface, $\tilde{N}^1_1 = \tilde{D}_{ox}\partial \tilde{c}^1/\partial \tilde{x}|_{\tilde{x}=1}$, which can only be calculated from the solution of Eqs. 7, 8. Thus, iterations are unavoidable: first, Eq. 12 is solved setting $\tilde{N}^1_1 = -r_\sigma \partial \tilde{\eta}^1/\partial \tilde{x}$, i.e., assuming that the flux $\tilde{N}^1_1$ is equal to the perturbation of the local current density. This is equivalent to the assumption that the oxygen transport in the CCL is fast. With $\tilde{c}^1_h$ at hand, we can solve the system 7, 8 and update the flux $\tilde{N}^1_1$. These iterations are repeated until the desired accuracy of the total impedance is achieved. Typically 2 to 3 iterations are necessary to reach the accuracy of Z_{cell} about 0.01%. It is important to note that in Eq. 12, the flux $\tilde{N}^1_1$ and the parameter $\tilde{D}_b$ depend on the coordinate $\tilde{z}$. Thus, in the parallel implementation of the model, all the local parameters $\tilde{N}^1_1$ and $\tilde{D}_b$ must be distributed over all the processes.

The fitting codes have been written in Python. To take advantage of modern multi–core CPUs, parallel codes have been developed using the standard message passing interface library *mpi4py*. The cell is separated into N virtual segments and N processes are generated, so that each process solves one predefined segment. Typically (though not necessary) $N = 10$, as in our experiments. The complex Eqs. 7 and 8 have been converted into equations for real and imaginary parts of the unknowns. The resulting system of four real equations as well as Eq. 17 have been solved using the boundary–value problem solver *solve_bvp* from the Python Scipy library. Eq. 12 has also been split into two real equations for the real and imaginary parts of $\tilde{c}^1_h$, and this system has been solved using the Cauchy problem solver *odeint* from the Scipy library. On each iteration step, the processes exchange the data on $\tilde{N}^1_1$ and $\tilde{D}_b$ to calculate common for all the processes function $\tilde{c}^1_h(\tilde{z})$ from Eq. 12. The local data for $\tilde{N}^1_1$ and $\tilde{D}_b$ have been interpolated by cubic spline to get continuous functions of $\tilde{z}$ in Eq. 12.

Local and cell models.—The spectra fitting has been done with the Scipy least–squares routine *least_squares* and the method *trf*.[35] In the LIM, each process fits the LIM to the individual impedance spectrum of its own segment. Five parameters have been declared as fitting ones: b, σ_0, C_{dl}, D_{ox} and D_b. Each process, thus, finds five optimal parameters providing the best fit of the model segment spectrum to the experimental local spectrum.

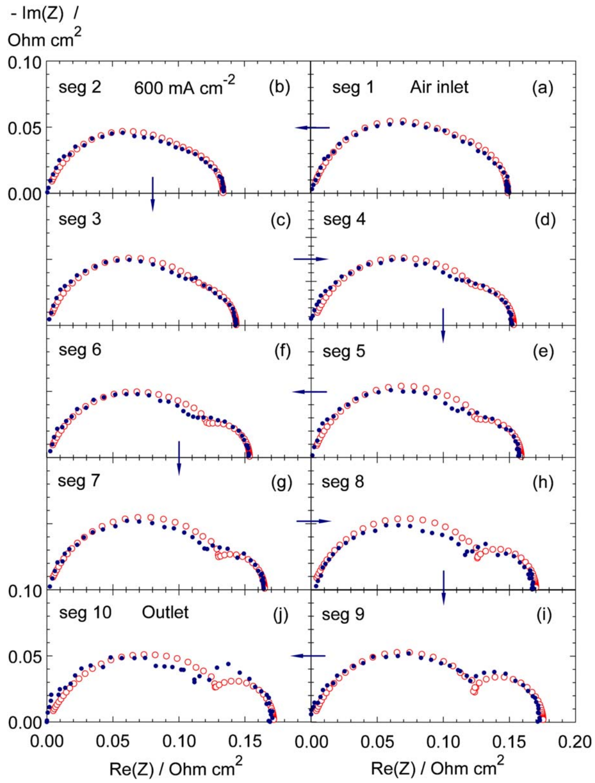

Figure 3. Local experimental (points) and fitted LIM (open circles) spectra for the cell current density of 600 mA cm^{-2}.

Technically, the largest difficulty in the LIM is information exchange between the processes. Local segment impedance depends on the perturbed oxygen fluxes at the channel/GDL interface (the right side of Eq. 12) in all the other segments, and hence for each frequency, the segment processes must exchange their values of oxygen fluxes. This can only be done if the set of experimental frequencies for all the segments is the same. To fulfill this requirement, the set of frequencies used in the LIM has been limited by the range of 0.1 to 10^3 Hz. Within this frequency range, the experimental impedance of all the segments does not exhibit inductive features.

In the CIM, the cell impedance, Eq. 16, is fitted to the experimental spectrum of the whole cell. As in the LIM, each process calculates impedance of its own segment; however, only the whole cell impedance 16 is fitted to the experimental spectrum. In other words, the global merit function is formulated in the space of $5N$ parameters and for $N = 10$ we get an optimization problem with 50 parameters.

Curve fitting is an iterative process; in all the cases, the iterations started from some reasonable uniform distribution of parameters along the channel. Model run times are indicated below for the PC with the 2.4 GHz quad–core processor and ten segments. The typical run time of the LIM for a set of the local spectra corresponding to a single current density is about 30 min, while the CIM requires from 2 to 4 hours to fit a single cell spectrum. This is not surprising, as the CIM searches the minimum of the merit function in a space of 50 parameters, while each process of the LIM performs this work in a space of 5 parameters. Note that with the most recent 8–core/4.2 GHz processors, we may expect four– to tenfold acceleration of the code.

Results and Discussion

Before fitting, all the whole cell spectra have been preprocessed according to the following procedure. The most high–frequency points

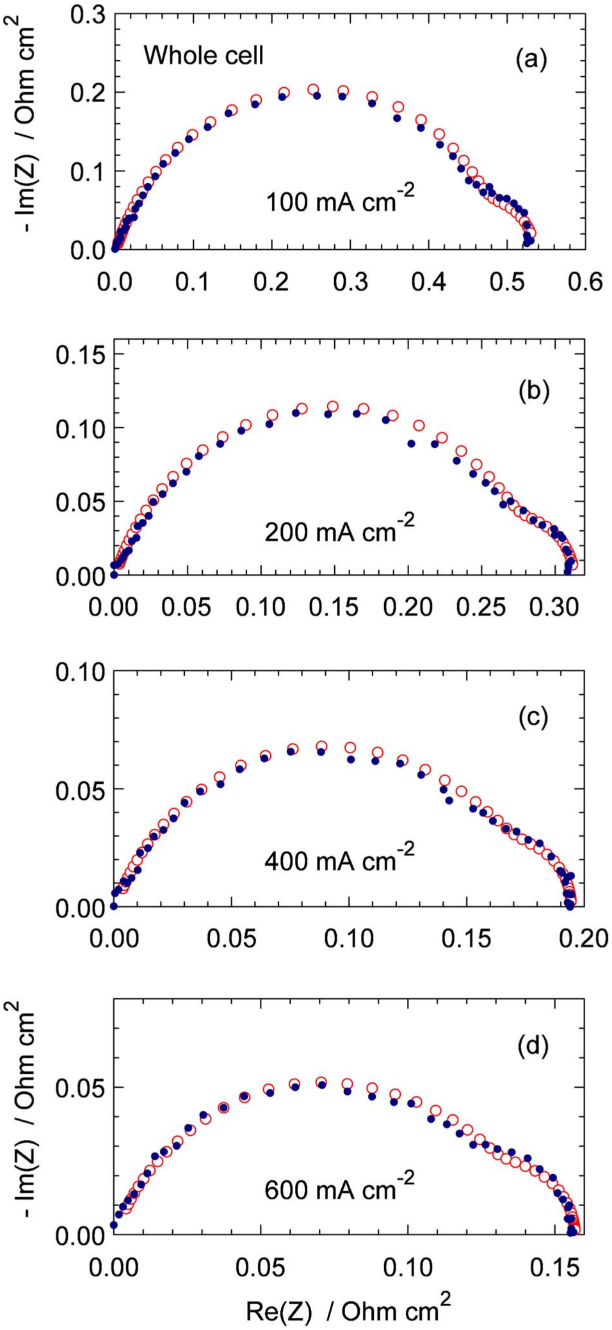

Figure 4. Experimental (dots) and fitted CIM (open circles) spectra of the whole cell for the indicated cell current densities.

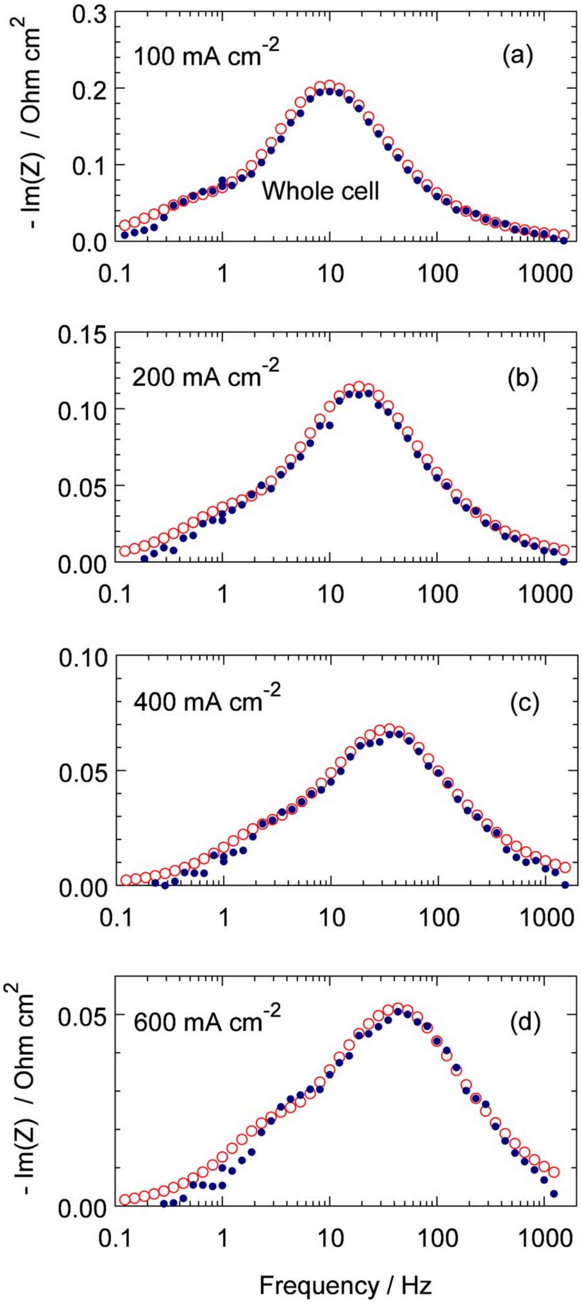

Figure 5. Bode plots of the experimental (dots) and fitted CIM (open circles) spectra of the whole cell for the indicated cell current densities.

with $\mathrm{Im}\,(Z) > 0$ have been discarded, as in this frequency range, the impedance is strongly affected by cables inductance. Further, the real part of the remaining leftmost point has been subtracted from the real parts of all the other points, i.e., the spectrum has been shifted to the left along the real axis in order to subtract the contribution of ohmic resistivities in the cell.

As discussed above, the LIM requires that the set of frequencies for all the segments would be the same. Thus, the real part of the impedance at the largest selected frequency of 1 kHz have been subtracted from all the local spectra to remove the contribution of ohmic resistivities.

Local experimental and fitted LIM spectra for the cell current density of 100 mA cm^{-2} are shown in Figure 2. As can be seen, the quality of fitting is quite good, though in the last segments 7 to 10 it lowers in the low–frequency (LF) range. Far from the cathode channel inlet, the LF loop exhibiting oxygen transport impedance in the channel is not fitted well. Possible reason is that true two–dimensional effects, which are ignored in the model (e.g., under–rib oxygen transport) may affect the oxygen concentration in the last segments. Surprisingly, at the cell current of 600 mA cm^{-2}, the quality of LF arc fitting in the last segments is better (Figure 3).

Fitted CIM and experimental spectra of the whole cell are compared in Figure 4 for the cell currents of 100 to 600 mA cm^{-2}. Bode plots of the imaginary part of the model and experimental impedance vs the frequency of applied signal are shown in Figure 5. As can be seen, with the growth of cell current density, due to noise of the experimental spectra, the quality of spectra fitting in the frequency range below 1–3 Hz gets worse (Figure 5). We attribute the noise of experimental

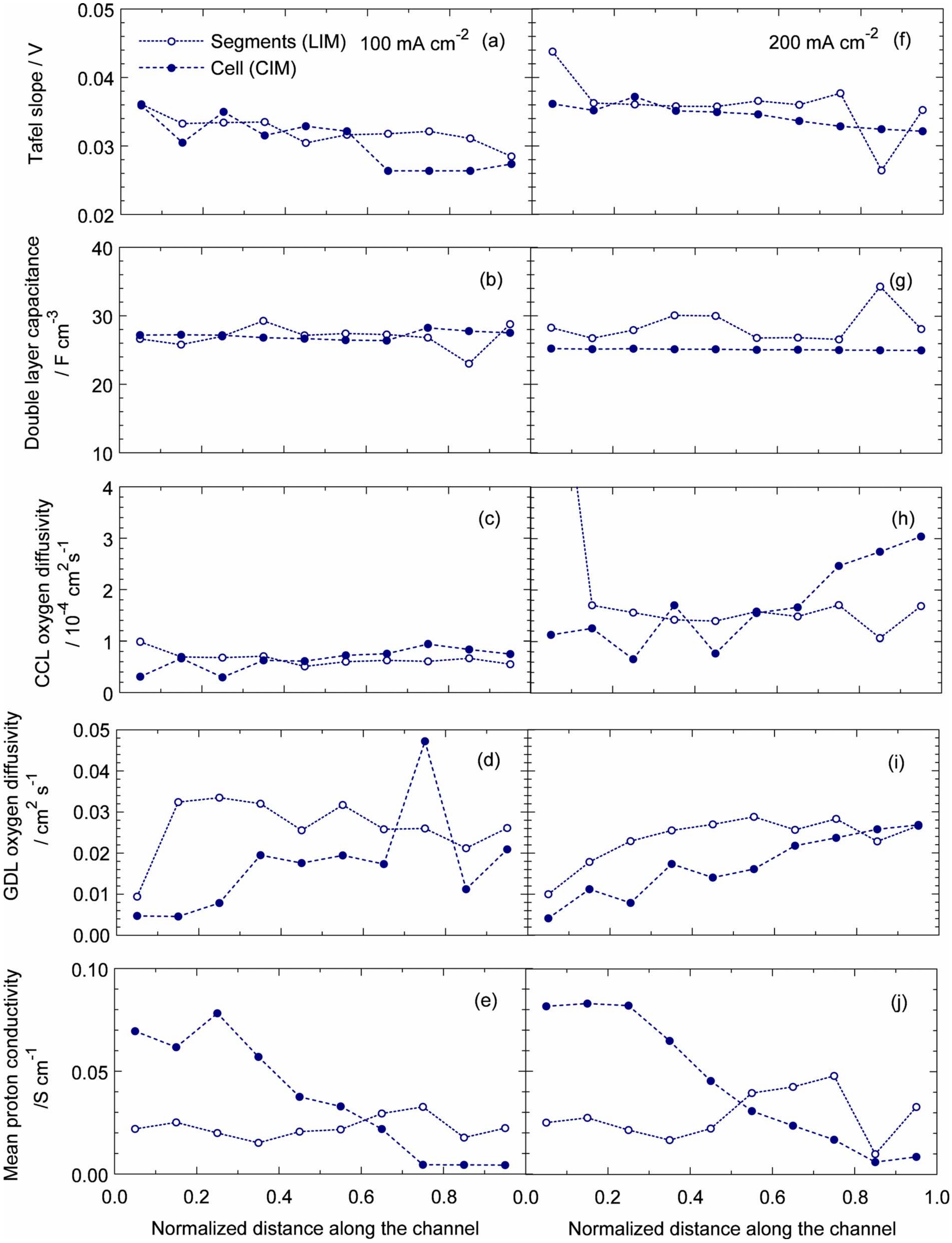

Figure 6. The ORR Tafel slope, the double layer capacitance, and the cell transport parameters resulted from fitting the local spectra (open points) and of the whole cell spectrum (solid points). The cell current density is 100 mA cm^{-2} (left column) and 200 mA cm^{-2} (right column).

spectra in this frequency range to transport of liquid water in the GDL and channel.

The distribution of cell parameters along the air channel resulted from the LIM and CIM are compared in Figures 6 and 7. The parameters obtained from the LIM are considered as reference values. Comparing the curves in Figure 6, we can conclude that the CIM well reproduces the shapes of the Tafel slope, double layer capacitance, and CCL oxygen diffusivity. At $J = 200$ mA cm^{-2}, the CIM well

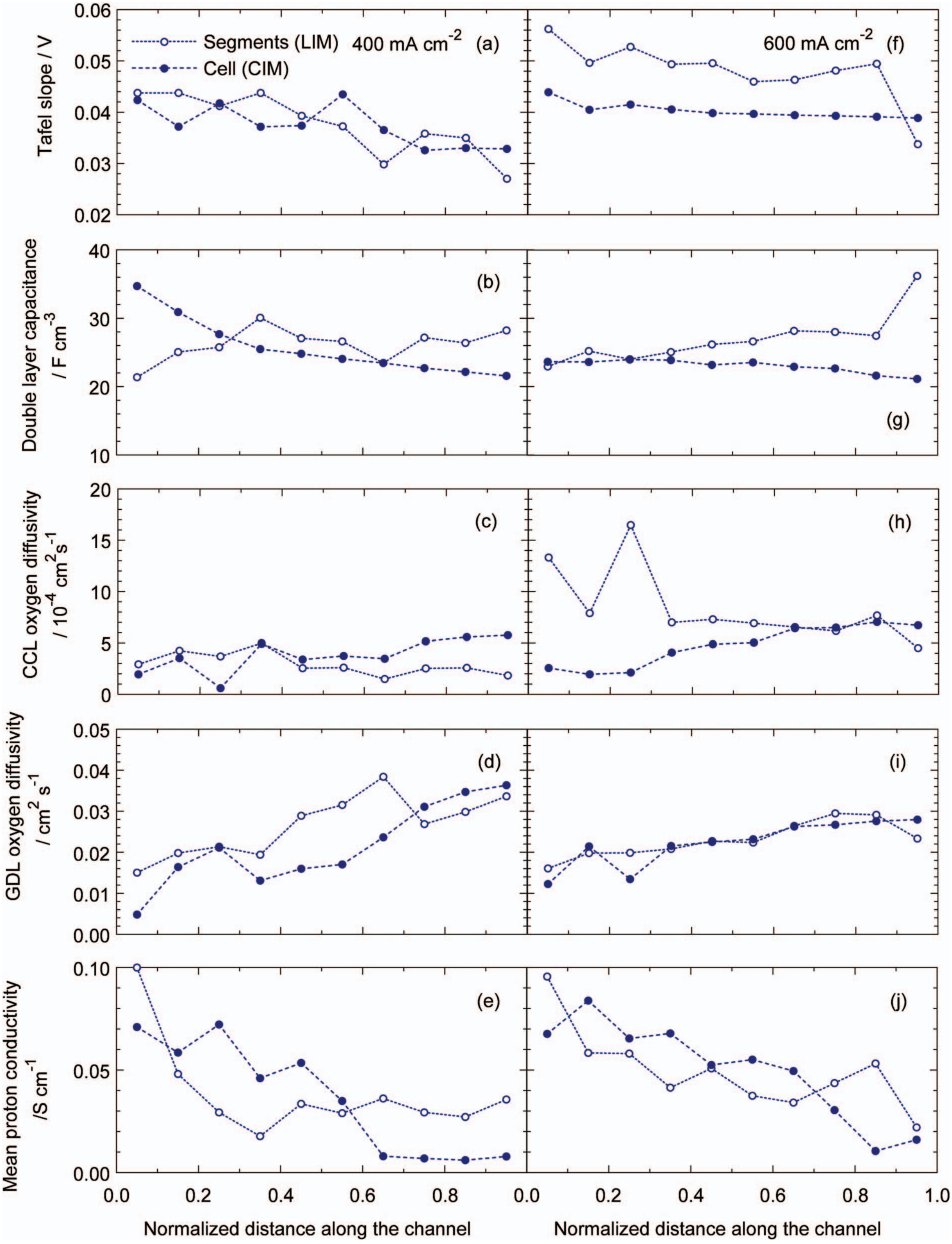

Figure 7. The ORR Tafel slope, the double layer capacitance, and the cell transport parameters resulted from fitting the local spectra (open points) and of the whole cell spectrum (solid points). The cell current density is 400 mA cm^{-2} (left column) and 600 mA cm^{-2} (right column).

reproduces the growing along the channel GDL oxygen diffusivity (Figure 6i). The largest gap (by a factor of three) between the two models exhibit the CCL proton conductivity in Figures 6e and 6j and the GDL oxygen diffusivity in Figure 6d.

At higher cell currents, all the shapes resulted from the two models are in good agreement, excluding the Tafel slope in Figure 7f, where CIM underestimates the Tafel slope by about 20%. Note that the CIM well describes the growth of the GDL oxygen diffusivity along the channel in Figures 7d, 7i and the decay of the CCL proton conductivity along z in Figures 7e, 7g. The origin of this effect is not clear yet. Modestov et al. provided experimental evidence that at lower cell potentials, the CCL proton conductivity increases due to protons released in oxidation of acidic species on the surface of carbon support.[36] Thus, one may speculate that this process is hindered by the liquid water, which is expected to accumulate in the CCL of remote segments.

Figures 6, 7 also show that the mean over channel length values of σ_p and D_{ox} increase with the cell current density. This effect has been reported in our previous work.[32] The growth of σ_p with J could be explained as discussed above, while the growth of D_{ox} with J yet has no explanation. It should be noted that this trend is repeatedly observed in various MEAs, including much thicker systems with non–Pt catalyst (to be published elsewhere). It is worth noting here that the HFR variation along the channel does not exhibit any clear trend and it is rather marginal (less than 20%) for all the cell currents.

Local impedance spectroscopy is a unique method for measuring local PEMFC parameters along the channel at working cell conditions; no other technique could provide comparable amount of information from a single run. Baker et al. reported a rather sophisticated limiting current density (LCD) method for measuring components of the oxygen transport resistivity in a differential PEMFC.[37] Similar technique has been used by Reshetenko and St-Pierre to separate the contributions of oxygen transport in the GDL and CCL.[38] However, the LCD method cannot be applied for the standard cell operating conditions: it requires diluted oxygen stream with low O_2 concentrations (below 5%) and high oxidant flow rates. In addition, the regime of CCL operation at the limiting cell current $j_{\lim}$ is not clear. Presumably, due to oxygen exhaustion, only a very thin sub–layer at the CCL/GDL interface converts $j_{\lim}$. In this situation, the CCL oxygen transport coefficients determined by the LCD correspond to this thin sub–layer only. To the best of our knowledge, measurements of D_{ox} and D_b in operating fuel cell are not available in literature. Liu et al. [39,40] reported an impedance spectroscopy study of proton conductivity of PEMFC cathodes with variable ionomer to carbon (I/C) ratio and under variable humidity. However, their measurements have been performed without oxygen in the electrodes (in the H_2/N_2 regime); comparison with the results above would hardly be correct.

The great advantage of the CIM is that it does not require cell segmentation; this model recovers the shapes of local cell parameters using information from a single impedance spectrum of the whole cell. Our experience shows that application of CIM to standard PEMFCs with Pt/C–based electrodes operated at medium to large currents (above 200–300 mA cm^{-2}) gives quite reasonable estimate of the local parameters. However, in the systems with low transport losses in the channel, the CIM fails. The reason is clear from Figure 1: if $|Z_h|$ is much smaller, than $|Z_{loc}|$, the circuit in Figure 1 degrades to the parallel connection of N impedances Z_{loc} and the exact location of each Z_{loc} cannot be resolved. This explains poor CIM–shapes of the CCL proton conductivity in the low–current Figures 6e and 6j, as at low currents, the relative weights of $|Z_h|$ in the total cell impedance decreases. Thus, a prerequisite for successful CIM application is that the oxygen transport impedance in the channel should be not small as compared to other impedances in the system.

Conclusions

We report a model for fitting local impedance spectra from the segmented fuel cell. This local impedance model (LIM) is used to validate our recent model for recovery of local parameters from a single spectrum of the whole fuel cell (cell impedance model, CIM).[23] Comparison of the results from the LIM and CIM shows that the CIM gives reasonably good shapes of the local cell parameters along the cathode channel, provided that the oxygen transport impedance in the channel is not small.

Both models indicate the decay of the CCL proton conductivity in the segments located close to the channel outlet at the cell current density $J = 400$ and 600 mA cm^{-2}. Following experimental study of Modestov et al.,[36] one may speculate that at lower cell potentials, the CCL proton conductivity increases due to oxidation of acidic species attached to the carbon surface. This process could be hindered by accumulation of liquid water in the CCL, which is expected to occur close to the air channel outlet in the cell. Further, both the models indicate large growth of the CCL oxygen diffusivity with the cell current density. The origin of these effects requires further investigations.

Acknowledgments

T. Reshetenko gratefully acknowledges funding from US Office of Naval Research (N00014-15-1-0028) and US Army Research Office (W911NF-15-1-0188). The authors are thankful to Günter Randolf and Jack Huizingh for valuable help in the system operation and the Hawaiian Electric Company for ongoing support of the Hawaii Sustainable Energy Research Facility.

List of Symbols

$\tilde{}$	Marks dimensionless variables
b	ORR Tafel slope, V
C_{dl}	Double layer volumetric capacitance, F cm^{-3}
c	Oxygen molar concentration, mol cm^{-3}
c_{ref}	Reference oxygen concentration (at the channel inlet), mol cm^{-3}
D_b	Effective oxygen diffusion coefficient in the GDL, cm^2 s^{-1}
D_{ox}	Effective oxygen diffusion coefficient in the CCL, cm^2 s^{-1}
F	Faraday constant, C mol^{-1}
f	Regular frequency, Hz
J	Mean cell current density, A cm^{-2}
j	Local proton current density in the CCL, A cm^{-2}
j_0	Local cell current density, A cm^{-2}
h	Channel depth, cm
i	Imaginary unit
i_*	Volumetric exchange current density, A cm^{-3}
L	Channel length,cm
l_b	GDL thickness, cm
l_t	Catalyst layer thickness, cm
r_b	$r_b = b/b_*$
r_{dl}	$r_{dl} = C_{dl}/C_{dl}^*$
r_σ	$r_\sigma = \sigma_0/\sigma_*$
s	Proton conductivity shaping function, Eq. 4
t	Time, s
v	Flow velocity in the cathode channel, cm s^{-1}
x	Coordinate through the cell, cm
Z	Impedance, Ω cm^2
z	Coordinate along the air channel, cm

Greek

β	Characteristic scale of the proton conductivity variation along $\tilde{x}$, Eq. 4
ε	Dimensionless Newman's reaction penetration depth, Eq. 11
η	ORR overpotential, positive by convention, V
λ	Air flow stoichiometry
μ	Dimensionless parameter, Eq. 11
ξ	Dimensionless parameter, Eq. 14
σ_0	CCL proton conductivity at the membrane/CCL interface, Ω^{-1} cm^{-1}
$\tilde{\Omega}$	Reduced dimensionless frequency, Eq. 11
ω	Angular frequency ($\omega = 2\pi f$), s^{-1}

Subscripts

0	Membrane/CCL interface
1	CCL/GDL interface
b	GDL
h	Air channel
seg	Segment impedance

t	Catalyst layer
$*$	Characteristic value

Superscripts

0	Steady–state value
1	Small–amplitude perturbation

ORCID

Tatyana Reshetenko https://orcid.org/0000-0002-4552-062X
Andrei Kulikovsky https://orcid.org/0000-0003-1319-576X

References

1. K. Takanohashi, T. Suga, M. Uchida, T. Ueda, Y. Nagumo, J. Inukai, H. Nishide, and M. Watanabe, "Simultaneous visualization of oxygen partial pressure, current density, and water droplets in serpentine fuel cell during power generation for understanding reaction distributions," *J. Power Sources*, **343**, 135 (2017).
2. M. E. Orazem and B. Tribollet, *Electrochemical Impedance Spectroscopy*, 2nd Edition. Wiley, New–York, 2017.
3. A. Kulikovsky, *Analytical Models for PEM Fuel Cell Impedance*. Self–publishing, Eisma, 2018. ISBN 9781521470749. URL https://www.amazon.com/Andrei-Kulikovsky/e/B00KBW7KVY.
4. T. E. Springer, T. A. Zawodzinski, M. S. Wilson, and S. Gottesfeld, "Characterization of polymer electrolyte fuel cells using AC impedance spectroscopy," *J. Electrochem. Soc.*, **143**, 587 (1996).
5. M. Eikerling and A. A. Kornyshev, "Electrochemical impedance of the cathode catalyst layer in polymer electrolyte fuel cells," *J. Electroanal. Chem.*, **475**, 107 (1999).
6. J. P. Meyers, M. Doyle, R. M. Darling, and J. Newman, "The impedance response of a porous electrode composed of intercalation particles," *J. Electrochem. Soc.*, **147**, 2930 (2000).
7. Y. Bultel, L. Genies, O. Antoine, P. Ozil, and R. Durand, "Modeling impedance diagrams of active layers in gas diffusion electrodes: Diffusion, ohmic drop effects and multistep reactions," *J. Electroanal. Chem.*, **527**, 143 (2002).
8. F. Jaouen and G. Lindbergh, "Transient techniques for investigating mass–transport limitations in gas diffusion electrode," *J. Electrochem. Soc.*, **150**, A1699 (2003).
9. Q. Guo and R. E. White, "A steady–state impedance model for a PEMFC cahode," *J. Electrochem. Soc.*, **151**, E133 (2004).
10. Y. Bultel, K. Wiezell, F. Jaouen, P. Ozil, and G. Lindbergh, "Investigation of mass transport in gas diffusion layer at the air cathode of a PEMFC," *Electrochimica Acta*, **51**, 474 (2005).
11. D. Gerteisen, A. Hakenjos, and J. O. Schumacher, "AC impedance modeling study on porous electrodes of proton exchange membrane fuel cells using an agglomerate model," *J. Power Sources*, **173**, 346 (2007).
12. A. A. Franco, P. Schott, C. Jallut, and B. Maschke, "A multi-scale dynamic mechanistic model for the transient analysis of PEFCs," *Fuel Cells*, **7**, 99 (2007).
13. I. A. Schneider, M. H. Bayer, and S. von Dahlen, "Locally resolved electrochemical impedance spectroscopy in channel and land areas of a differential polymer electrolyte fuel cell," *J. Electrochem. Soc.*, **158**, B343 (2011).
14. O. Shamardina, M. S. Kondratenko, A. V. Chertovich, and A. A. Kulikovsky, "A simple transient model for a high temperature PEM fuel cell impedance," *Int. J. Hydrogen Energy*, **39**, 2224 (2014).
15. B. P. Setzler and Th. F. Fuller, "A physics–based impedance model of proton exchange membrane fuel cells exhibiting low–frequency inductive loops," *J. Electrochem. Soc.*, **162**, F519 (2015).
16. C. Bao and W. G. Bessler, "Two–dimensional modeling of a polymer electrolyte membrane fuel cell with long flow channel. Part II. physics–based electrochemical impedance analysis," *J. Power Sources*, **278**, 675 (2015).
17. A. Baricci and A. Casalegno, "A simple analytical approach to simulate the electrochemical impedance response of flooded agglomerates in polymer fuel cells," *Electrochimica Acta*, **157**, 324 (2015).
18. S. Chevalier, C. Josset, and B. Auvity, "Analytical solution for the low frequency polymer electrolyte membrane fuel cell impedance," *J. Power Sources*, **407**, 123 (2018).
19. S. J. C. Cleghorn, C. R. Derouin, M. S. Wilson, and S. Gottesfeld, "A printed circuit board approach to measuring current distribution in a fuel cell," *J. Appl. Electrochem.*, **28**, 663 (1998).
20. D. J. L. Brett, S. Atkins, N. P. Brandon, V. Vesovic, N. Vasileadis, and A. Kucernak, "Localized impedance measurements along a single channel of a solid polymer fuel cell," *Electrochem. Solid State Lett.*, **6**, A63 (2003).
21. T. V. Reshetenko, G. Bender, K. Bethune, and R. Rocheleau, "A segmented cell approach for studying the effects of serpentine flow field parameters on PEMFC current distribution," *Electrochimica Acta*, **88**, 571 (2013).
22. E. Engebretsen, G. Hinds, Q. Meyer, T. Mason, E. Brightman, L. Castanheira, P. R. Shearing, and D. J. L. Brett, "Localised electrochemical impedance measurements of a polymer electrolyte fuel cell using a reference electrode array to give cathode–specific measurements and examine membrane hydration dynamics," *J. Power Sources*, **382**, 38 (2018).
23. T. Reshetenko and A. Kulikovsky, "A model for extraction of spatially resolved data from impedance spectrum of a PEM fuel cell," *J. Electrochem. Soc.*, **165**, F291 (2018).
24. T. Reshetenko and A. Kulikovsky, "Comparison of two physical models for fitting PEM fuel cell impedance spectra measured at a low air flow stoichiometry," *J. Electrochem. Soc.*, **163**, F238 (2016).
25. T. Reshetenko and A. Kulikovsky, "PEM fuel cell characterization by means of the physical model for impedance spectra," *J. Electrochem. Soc.*, **162**, F627 (2015).
26. T. V. Reshetenko, G. Bender, K. Bethune, and R. Rocheleau, "Systematic study of back pressure and anode stoichiometry effects on spatial PEMFC performance distribution," *Electrochimica Acta*, **56**, 8700 (2011).
27. A. Kulikovsky and O. Shamardina, "A model for PEM fuel cell impedance: Oxygen flow in the channel triggers spatial and frequency oscillations of the local impedance," *J. Electrochem. Soc.*, **162**, F1068 (2015).
28. T. Reshetenko and A. Kulikovsky, "Impedance spectroscopy characterization of oxygen transport in low– and high–pt loaded PEM fuel cells," *J. Electrochem. Soc.*, **164**, F1633 (2017).
29. T. Reshetenko and A. Kulikovsky, "Impedance spectroscopy study of the PEM fuel cell cathode with nonuniform nafion loading," *J. Electrochem. Soc.*, **164**, E3016 (2017).
30. I. A. Schneider, S. A. Freunberger, D. Kramer, A. Wokaun, and G. G. Scherer, "Oscillations in gas channels. part i. the forgotten player in impedance spectroscopy in PEFCs," *J. Electrochem. Soc.*, **154**, B383 (2007).
31. I. A. Schneider, D. Kramer, A. Wokaun, and G. G. Scherer, "Oscillations in gas channels. ii. unraveling the characteristics of the low–frequency loop in air–fed PEFC impedance spectra," *J. Electrochem. Soc.*, **154**, B770 (2007).
32. T. Reshetenko and A. Kulikovsky, "Variation of PEM fuel cell physical parameters with current: Impedance spectroscopy study," *J. Electrochem. Soc.*, **163**(9), F1100 (2016).
33. S. Chevalier, C. Josset, and B. Auvity, "Analytical solutions and dimensional analysis of pseudo 2D current density distribution model in PEM fuel cells," *Renew. Energy*, **125**, 738 (2018).
34. T. Reshetenko and A. Kulikovsky, "On the distribution of local current density along the PEM fuel cell cathode channel," *Electrochem. Comm.*, **101**, 35 (2019).
35. scipy.optimize.least-squares, 2018. URL https://docs.scipy.org/doc/scipy/reference/generated/scipy.optimize.least-squares.html.
36. A. D. Modestov, A. V. Kapustin, V. B. Avakov, I. K. Landgraf, and M. R. Tarasevich, "Cathode catalyst layers with ionomer to carbon mass ratios in the range 0–2 studied by electrochemical impedance spectroscopy, cyclic voltammetry, and performance measurements," *J. Power Sources*, **272**, 735 (2014).
37. D. R. Baker, D. A. Caulk, K. C. Neyerlin, and M. W. Murphy, "Measurement of oxygen transport resistance in PEM fuel cells by limiting current methods," *J. Electrochem. Soc.*, **156**, B991 (2009).
38. T. V. Reshetenko and J. St-Pierre, "Separation method for oxygen mass transport coefficient in gas and ionomer phases in PEMFC GDE," *J. Electrochem. Soc.*, **161**, F1089 (2014).
39. Y. Liu, M. W. Murphy, D. R. Baker, W. Gu, C. Ji, J. Jorne, and H. A. Gasteiger, "Proton conduction and oxygen reduction kinetics in PEM fuel cell cathodes: Effects of ionomer-to-carbon ratio and relative humidity," *J. Electrochem. Soc.*, **156**, B970 (2009).
40. Y. Liu, W. Gu, D. R. Baker, J. Jorne, and H. A. Gasteiger, "Proton conduction in pem fuel cell cathodes: Effects of electrode thickness and ionomer equivalent weight," *J. Electrochem. Soc.*, **157**, B1154 (2010).